Zhongchen Zhang
Laboratory for Alternative Energy Conversion (LAEC),
School of Mechatronic Systems Engineering,
Simon Fraser University,
250-13450 102 Avenue,
Surrey, BC V3T 0A3, Canada

Michael Collins
Solar Thermal Research Laboratory (STRL),
Department of Mechanical and Mechatronics Engineering,
University of Waterloo,
200 University Ave. W.,
Waterloo, ON N2 L 3G1, Canada

Eric Lau
Department of Engineering,
Delta-Q Technologies,
3755 Willingdon Ave.,
Burnaby, BC V5G 3H3, Canada

Chris Botting
Department of Research,
Delta-Q Technologies,
3755 Willingdon Ave.,
Burnaby, BC V5G 3H3, Canada

Majid Bahrami[1]
Laboratory for Alternative Energy Conversion (LAEC),
School of Mechatronic Systems Engineering,
Simon Fraser University,
250-13450 102 Avenue,
Surrey, BC V3T 0A3, Canada
e-mail: mbahrami@sfu.ca

The Role of Anodization in Naturally Cooled Heat Sinks for Power Electronic Devices

Effect of anodization on the thermal performance of naturally cooled heat sinks in power electronic devices made of die-cast aluminum alloy A380 and machined aluminum alloy 6061 was investigated experimentally and numerically. Various types of anodization were examined with different thickness of anodic aluminum oxide layer (AAO), pore size distributions, and surface coloring conditions. A customized natural convection and thermal radiation experimental chamber was built to measure the cooling capacity and heat sink temperatures. A 3D numerical model was also developed and validated against the collected data to provide more details into the contribution of the radiation heat transfer. The total emittance of the anodized samples was determined by a Fourier transform infrared reflectometer (FTIR) spectroscopy method. The results show a significant improvement in total hemispherical emissivity from 0.14 to 0.92 in anodized die-cast aluminum samples. This increase resulted in a considerable reduction in overall thermal resistance, up to 15%; where up to 41% of the total heat dissipation was contributed by thermal radiation. In spite of the rather distinguishable surface morphologies, the measurements suggested that thermal emissivity of the anodized die-cast Al A380 and Al alloy 6061 samples were in the same range. [DOI: 10.1115/1.4046309]

Keywords: anodization, thermal radiation, heat sinks, natural convection, power electronics, die-cast aluminum

1 Introduction

With the ever-increasing cooling demands coupled miniaturization trend in semiconductor devices, thermal management plays a critical role in the power electronics industry. More than half of failures in modern electronics are associated with inadequate temperature control and thermal regulation [1]. The mean time between failures (MTBFs) can be reduced exponentially when operations are maintained under maximum allowable temperature [2]. Among all the cooling methods, passively cooled heat sinks have been extensively used for heat removal in power electronic equipment due to several advantages including noise-free operation, zero-parasitic power consumption, and high reliability. However, it provides much less heat rejection capacity compared to its counterpart, actively cooled heat sinks, which greatly limits its universal applications, particularly in high power semiconductor devices. Thus, improving the cooling capability of naturally cooled heatsinks is desired, in particular for efficient and reliable power electronic products.

The overall heat transfer from a naturally cooled heat sink occurs via natural convection and thermal radiation. Several studies on passively cooled devices indicated that: (i) the radiation heat transfer contribution is notable; and (ii) there is significant potential to improve the overall heat transfer via radiation regardless of the fin geometries [3–5].

The majority of the available studies in the literature are either experimental or numerical investigations. Edwards and Chaddock [3] are among the earliest to report the significance of thermal radiation, where they concluded that one-third of the overall passive heat transfer in an extended cylindrical surface was contributed by radiation with a surface thermal emissivity close to 0.99. Following studies further confirmed the critical role of thermal radiation. Table 1 provides a review on the topic of thermal radiation from passively cooled heat sinks.

The radiative heat transfer between heat sink surfaces to the ambient can be calculated as

$$Q_r = \sigma\varepsilon\left(T_w^4 - T_a^4\right)\sum_{i=1}^{n} A_i F_{i\to\infty} \tag{1}$$

where σ is the Stefan-Boltzmann constant (5.67×10^{-8} $\mathrm{W \cdot m^{-2} \cdot K^{-4}}$), ε is the surface thermal emissivity, A is the surface area, and F is the view factor from the surface to the ambient, respectively. The surface emissivity is a key parameter depending on surface treatment, while heat dissipating area and view factor are generally associated with heat sink geometry, which is often dictated by the product design.

Anodization is often considered as the most common and cost-effective surface finishing method to alter the surface emissivity

[1]Corresponding author.

Contributed by the Heat Transfer Division of ASME for publication in the Journal of Heat Transfer. Manuscript received July 24, 2019; final manuscript received December 19, 2019; published online March 13, 2020. Editor: Portonovo S. Ayyaswamy.

Table 1 Literature review on the thermal radiation from finned heat sinks

Ref.	Approach	Fin geometry	Surface emissivity	$Q_r/Q(\%)$
Edwards and Chaddock [3]	Experimental	Cylindrical	0.99 Polished	33 10–20
Sparrow and Vemuri [6]	Experimental analytical	Cylindrical	0.82	25–45
Rao and Venkateshan [4]	Experimental numerical	Rectangular	0.05–0.85	25–40
Rao et al. [7]	Numerical	Rectangular	0.05–0.85	36–50
Yu et al. [8]	Experimental analytical	Rectangular	0.8	27
Tamayol et al. [9]	Experimental analytical	Rectangular	0.75	50
Guglielmini et al. [5]	Experimental	Staggered	0.05–0.85	25–40
Aihara et al. [10]	Experimental	Cylindrical	0.9	19–48

for aluminum and its alloys, which is well adopted throughout the industry. It is an electrochemical process that converts the original aluminum surface into a thin anodic aluminum oxide (AAO) film. In general, the anodization type (barrier-type and porous-type) of AAO film depends on the nature of electrolyte during the anodizing process. In particular, the porous-type has received considerable attention and has extensive application in practice. Attributed to its structure, AAO films have become a perfect base or substrate for electroplating, painting, and semipermanent decorative coloration [11]. Moreover, porous-type AAO films yielded by the acidic anodization offer many superior engineering properties such as excellent hardness, abrasion, and corrosion resistance [12]. In particular, the mechanical strength of AAO layers is of great interests in various applications [13–15].

The US Military specification (MIL-A-8625F) [16] categorizes the anodic coating for aluminum and its alloy into three types and two classes. Type I (chromic acid anodizing) can generate an ultrathin film ($\leq 17\ \mu$m) but with optimal properties for dye adhesion, and resisting corrosion. However, it is only applied to the surfaces where high precision is required such as aerospace and military industries, and its acidic residue poses less risk to metal fatigue compared with sulfuric acid despite the negative environmental impact of the by-products from the process. Nevertheless, type II (sulfuric acid anodizing) and type III (hard anodic coating) are more preferred in conventional engineering applications. Type II anodizing features a thinner film ($\leq 25\ \mu$m) to better serve the cosmetic purposes while type III (hard coat) anodizing, as its name suggested, is often implemented where higher wear and corrosion resistance are demanded with the assistance of a relatively thicker AAO layer ($\leq 115\ \mu$m).

The superior thermal radiative properties of AAO layer are also noticed by previous researches. In particular, in space application, thermal radiation is the only method to dissipate the waste heat into a vacuum environment. National Aeronautical Space Administration (NASA) performed a series of investigations of the thermal radiative properties of anodized aluminum as thermal control coatings in spacecraft design [17–19]. They found that the thermal radiative properties of anodized aluminum are promising, i.e., low solar absorptance and high thermal emittance, but such radiative properties highly depend on the electrolytes and AAO film thickness. Degradation of anodized layer in long-duration orbital exposure experiment was observed [20,21]. Furthermore, subsequent studies focused on the variety of aluminum alloys and potential adjustments to the anodizing procedures that may have a profound influence on overall thermal emissivity. Siva Kumar et al. [22] proposed a new approach for a white anodic oxide coating with special additive to the sulfuric acid bath and improved surface emittance up to 0.8 with lowest solar absorptance of 0.15 on aluminum alloy 2024. Lee et al. [23] compared the effect of different acidic electrolytes and sealing methods on thermal emissivity and found out that the oxalic acid with black sealing can result in the most substantial enchantment of thermal emissivity, up to 0.91, in aluminum alloy 1050. Klampfl [24] performed a parametric study of anodized 5657 aluminum for thermal control purposes and developed a chemical model for sulfuric acid anodized (SAA) aluminum coating.

Our main goal is to understand the effect of anodization on the thermal radiative properties of die-cast aluminum alloy A380 and machined aluminum alloy 6061 as well as to establish an understanding of the impact of emissivity on the thermal radiative behavior in passively cooled heat sinks. Several sample naturally cooled heat sinks were fabricated, anodized, and tested under identical operating conditions. The thermal emittance of anodized samples in both die-cast Al and Al alloy 6061 were also determined. A numerical model developed in ANSYS FLUENT 17.2 was validated by the collected data and used to decouple the contribution of the thermal radiation from total heat transfer in such anodized naturally cooled heat sinks.

2 Sample Preparation

The prepared samples can be divided into two categories based on the types of the aluminum alloys: (i) die-cast aluminum (A380) and (ii) the machined Al alloy 6061. It is impractical and of high cost to customize die-casting in small volumes. Thus, prepared die-cast aluminum plates (2.5 cm × 5.0 cm) for emissivity measurement are the flat fins chopped off an existing die-cast heat sink, Delta-Q Technologies IC650 battery charger heat sinks, shown in Fig. 1. The Al alloy 6061 sample plates (5.0 cm × 7.5 cm) are made from plates bought from a local BC vendor (metal supermarket) and machined in-house in our school. Several unprocessed IC650 naturally cooled heat sinks were also prepared and cleaned in advance for anodizing and testing. The dimensions, length (L), width (W), and height (H) of IC650 heat sink are 23 cm, 17 cm, and 7.5 cm (Fig. 1), respectively.

The anodization was performed in a local surface finishing treatment company (Spectral Finishing, Inc.) located in Surrey, BC. The anodizing process is followed by a procedure of cleaning, etching, acid desmutting, anodizing, coloring (optional), and sealing [25]. The objective of the first three steps is to remove any contamination on the surface during the manufacturing process

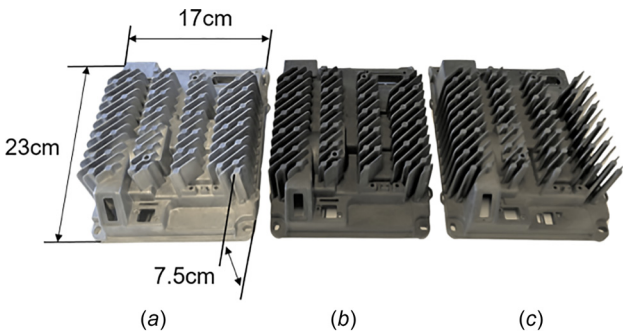

Fig. 1 IC650 heat sinks before and after various anodizing treatment, (*a*) bare; (*b*) type II-black; and (*c*) type III-clear

and etching away the original thin oxide layer that leaves a perfect aluminum substrate for anodizing. The coloring lets the newly formed porous AAO layer to absorb color pigments sufficiently to reach desired surface appearance. The last step, sealing, is a process of precipitating an additional layer of sealant, on top of the uncovered anodized surface to protect the pore structure to extend durability and avoid absorbing impurities. In some alloys with greater than 5% copper or 8% silicon, such as aluminum A380 (7.5–9.5% silicon), type III (hard coat) cannot be achieved [16]. In this case, the thickness of the AAO layer that formed on A380 alloys is confined to 25 μm for either type II or type III anodization. The metallic-based dyes are used for coloring and cold nickel fluoride sealing method was served as the last step to seal the uncovered AAO layer. Figure 1 shows a surface comparison before and after the anodization treatment. The surface darkness of dyed and clear samples is not significantly varied and the anodic layer itself shows this dull and gray color.

Both type II and type III anodized samples were prepared with different thickness of the anodic layer and surface color (clear or black). It should also be noted that the mentioned thickness is just used as a reference to differentiate the anodizing time in this context. Further efforts are required to perform investigation with precision to determine the accurate thickness of the anodic layer. In each group, at least two samples were anodized in the same condition to ensure the repeatability. Among the full treated sealed samples, the unsealed plates were also prepared with interests to investigate the effect of sealing layer on thermal emissivity, as well as to allow us to observe the pore distributions of the selected samples. The details of the prepared samples are listed in Table 2.

3 Experimental Setup

Thermal emissivity of anodized surfaces was measured using a 400 T infrared reflectometer from Surface Optics Corporation (SOC) available in Solar Thermal Research Laboratory (STRL) at the University of Waterloo. This is a Fourier transform infrared reflectometer (FTIR) designed for determining the spectral emittance of the samples in the range of wavelength from 2 μm to 25 μm. All measurements were performed under room temperature. Ideally, it would be preferable to keep the samples measured at an elevated temperature so as to be consistent with the actual working environment but conditioning the equipment has some challenges. The spectrometer measures the reflectance repeatability of $\pm 1\%$. The spectral measurement was performed in accordance with method C of ASTM E408-13 [26]. Detailed descriptions and comparison of SOC-400T can be found in Ref. [27].

The spectrometer was first calibrated by scanning the background room and recorded as zero spectrum. The reference spectrum was recording by measuring the reference surface made of polished gold with constant spectral reflectivity of 0.98 in the measured infrared range. The sample reflectance is measured and corrected by zero and reference spectrum, as

$$\gamma_{\text{sample}} = \frac{\gamma_{\text{measured}} - \gamma_{\text{zero}}}{\gamma_{\text{reference}} - \gamma_{\text{zero}}} \tag{2}$$

SOC 400T measures the directional-hemispherical reflectance directly and the IR beam is coming at samples from a near-normal direction (20 deg off normal) while the reflected signal is measured hemispherically. The detected reflectance can be reduced to hemispherical-hemispherical reflectance by a factor of pi. Thus, the spectral hemispherical emissivity can be easily calculated by being substrate by one as

$$\varepsilon_\lambda(\lambda, T) = \frac{E_\lambda(\lambda, T)}{E_{\lambda b}(\lambda, T)} = 1 - \frac{1}{\pi}\gamma_\lambda(\theta, \phi, T) \tag{3}$$

where E is emissive power and the subscripts λ and b denote the value in spectral and from the blackbody, respectively. θ and ϕ characterize the zenith angle and the azimuthal angle of the incident light. The total hemispherical emissivity is simply the quotient between the integration of spectral emissive power and of that from the blackbody at the same temperature in measured wavelength range and can be formulated as

$$\varepsilon(\lambda, T) = \frac{E(\lambda, T)}{E_b(\lambda, T)} = \frac{\int_{\lambda=2}^{\lambda=25} \varepsilon_\lambda(\lambda, T) E_{\lambda b}(\lambda, T) d\lambda}{\int_{\lambda=2}^{\lambda=25} E_{\lambda b}(\lambda, T) d\lambda} \tag{4}$$

All the samples were imaged with a field emission scanning electron microscopy (Nova Nano-SEM, Thermo Fisher Scientific) available in the 4D LABS at Simon Fraser University to capture the unique microstructures of anodic layers. The anodized samples were coated with 10 nm iridium using a high vacuum sputter system (EM ACE 600, Leica Microsystems) before imaging.

A custom-designed testbed was developed to perform steady-state natural convection and thermal radiation heat transfer tests. As an effort to reduce the flow disturbance and to provide a uniform radiation background, a test chamber ($0.5 \times 0.5 \times 0.5$ m^3) was built with 4 mm thick acrylic plastics. The surface emissivity of acrylic plastic is approximately 0.9 in the wavelength of infrared light with physical and thermal properties of density ($\rho = 1180$ kg·m^{-3}), thermal conductivity ($k = 0.2$ W·m^{-1}·K^{-1}), and specific heat ($c_p = 1470$ J·kg^{-1}·K^{-1}). Several ultrathin polyimide film heaters with pressure-sensitive adhesive were used at the base of the heat sink to mimic heat generation from electronic components. All heaters have a power density of 1.6 W·cm^{-2} (10 W·in^{-2}) and are of three sizes, i.e., 1.3 cm × 5.1 cm, 2.5 cm × 2.5 cm, and 2.5 cm × 5.1 cm. A programmable DC power supply (Chroma 62012 P-100-50) supplied electrical power. T-type (copper-constantan) thermocouples were used to monitor the temperature distribution along the heat sink base, chamber ambient, and chamber walls. A NI-9212 (National Instrument) temperature acquisition module and a NI-9229 (National Instrument) voltage analog input unit were connected to a compactDAQ

Table 2 Prepared samples with various types of anodization

Number of samples			Plates (A380)	Plates (machined 6061)	Heat sinks (A380)
Untreated			2	2	2
Type II sealed	Clear	15 μm	—	2	—
		20 μm	2	—	—
	Black	20 μm	—	2	—
		25 μm	4	—	2
Type III clear	Sealed	25 μm	4	—	2
		66 μm	—	2	—
	Unsealed	25 μm	2	2	—
		66 μm	—	2	—

(cDAQ-9174) chassis, which transfers the recorded temperature and voltage measurement to the external computer to complete the data acquisition. The sample battery charger heat sinks (IC650) were tested in the horizontal orientation as indicated in Fig. 2. A centimeter-thick wooden plate board was placed underneath the heat sink to prevent heat loss from the base. The front ports and gaps were also taped with aluminum foil to ensure airtight sealing for the internal region. Five ultrathin polyimide film heaters and fourteen thermocouples were installed to conduct these tests. The location of heaters and thermocouples can be found in Fig. 2, where T7 and T11 were attached on the chamber wall to monitor the wall temperature.

Thermal tests were performed in an open lab environment facing north, free of direct sunlight from the windows. The room temperature was steady and remained constant at 22 °C. Each heat sink was tested with various power levels from 20 W to 80 W. The steady-state condition was reached when the partial derivative of all temperatures with respect to time ($\partial T/\partial t$) was less than 0.001 °C for 30 mins. Each test was repeated three times to ensure the repeatability of the experimental results. The actual testbed is shown in Fig. 3.

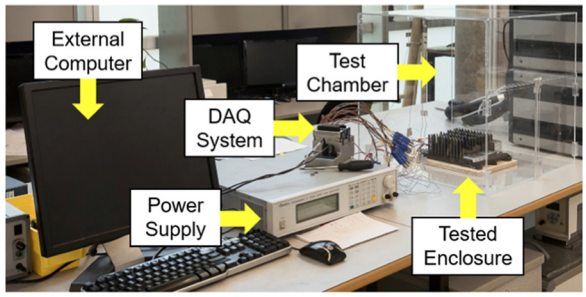

Fig. 3 Components of the experimental setup

4 Numerical Analysis

A new 3D conjugated heat transfer numerical model is developed in ANSYS FLUENT 17.2 to investigate both natural convection and thermal radiation. The governing equations in ambient air with Boussinesq approximation for density-temperature are listed below:

$$\nabla \cdot \mathbf{u} = 0 \tag{5}$$

$$\mathbf{u} \cdot \nabla \mathbf{u} = -\frac{1}{\rho_\infty}\nabla \tilde{P} + \upsilon \nabla^2 \mathbf{u} - g\beta(T - T_\infty)\hat{n} \tag{6}$$

$$\mathbf{u} \cdot \nabla T = \alpha \nabla^2 T \tag{7}$$

where $\hat{n}$ is the normal vector of the heat sink base and parallel to the gravity acceleration. ρ, μ, and α are the density, viscosity, and thermal diffusivity, respectively.

Since we only consider the radiative heat transfer between surfaces where any absorption, emission, and scattering effects in ambient air is ignored. The total heat flux leaving a surface i with incident radiation from surfaces j, for $j = 1, 2, 3, \ldots N$ [28]

$$q_{\text{out},k} = \varepsilon_i \sigma T_i^4 + \gamma_i \sum_{j=1}^{N} F_{ij} q_{\text{out},j} \tag{8}$$

where F_{ij} is the view factor between surface i and j and indicates the fraction of energy leaving surface j that incidents on surface i. γ is the surface reflectivity and can be calculated as $\gamma = 1 - \varepsilon$ using Kirchhoff's law of radiation. N represents the number of surfaces that interact with surface i and will shed radiation. The view factor between surface i and j is given by

$$F_{ij} = \frac{1}{A_i}\int_{A_i}\int_{A_j} \frac{\cos\varphi_i \cos\varphi_j}{\pi r^2}\eta_{ij} dA_i dA_j \tag{9}$$

where A and r are the surface area and distance. φ are the angle between the direction of radiation and surface normal. η_{ij} is determined by the visibility of dA_i and dA_j and equals to 1 if dA_i is visible to dA_j.

All solid walls, i.e., either heat sink surfaces or fluid domain walls, have the no-slip and nonpenetration boundary conditions. For the frontal interface of the heat sink that is in contact with ambient air, the boundary conditions were set via system coupling. The adiabatic boundaries were imposed on the back surfaces of the heat sink given that we assume heat can be only transferred out through the fins. Constant volumetric heat flux conditions were assumed to the heat generating components depending on the overall heat input into the systems resembling the actual experimental test. The chamber walls were isothermal during the tests; measured temperatures were imposed in the model. Because of the enclosed environment where heat

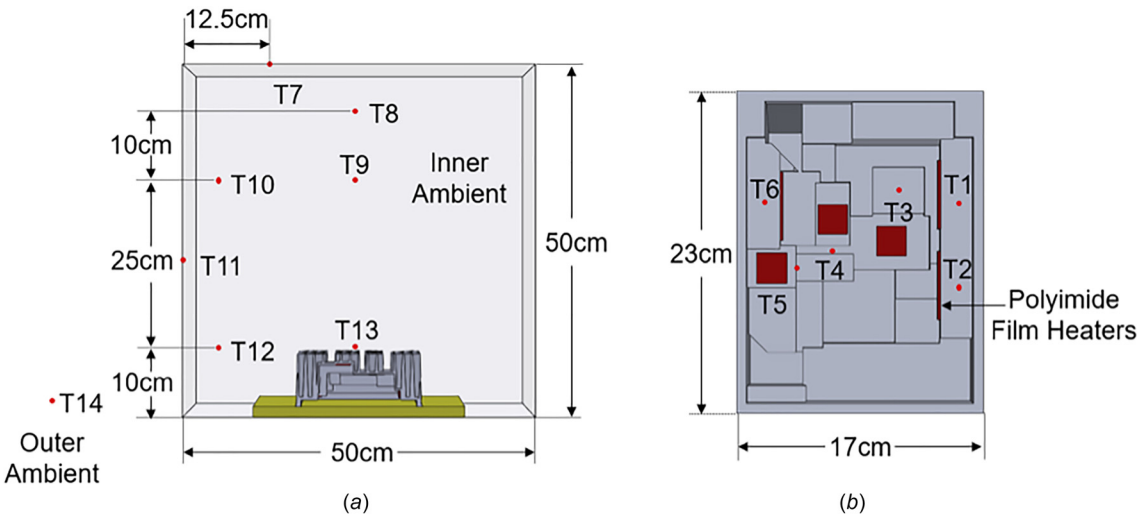

Fig. 2 Schematic of the experimental setup, including locations of thermocouples; (*a*) custom-built test chamber; (*b*) back view of the tested heat sink, heating components shown as squares

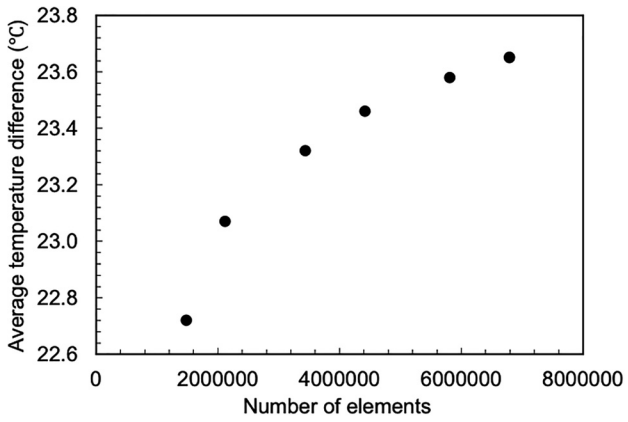

Fig. 4 Mesh independency study: average base temperature variation with respect to the number of meshing elements

accumulates and can only be dissipated by the convection and radiation from chamber walls, the chamber ambient should increase and settle on a new temperature when the system reaches steady-state. The measured total hemispherical emissivity values were used as surface emissivity for the heat sink surfaces. The chamber walls have a uniform surface emissivity of $\varepsilon = 0.9$ as previously mentioned.

The SIMPLE algorithm in FLUENT 17.2 was used to solve the set of governing equations. The momentum and energy term were discretized by the first-order accuracy Power Law scheme and the PRESTO (pressure staggering option) was adopted in the discretization of pressure terms. Because of the high nonlinearity and instability of the natural convective flow, under-relaxation factors (URF) have been adjusted to 0.35 in momentum terms with preset value for energy and pressure terms. The simulations were considered as converged when all the temperature variations within past 100 steps fall into the range of 1×10^{-4}. The convergence criterion for radiosity residual is 1×10^{-3}.

Figure 4 shows the mesh independency study results where the average heat sink base temperature difference slightly varies with the number of meshing elements with a thermal input of 40 W. As the number of elements increases from nearly 2,000,000 to 8,000,000, the temperature difference rises from 22.7 °C to 23.6 °C. Therefore, we took the finest mesh size of 1.5×10^{-3} and 1.2×10^{-2} on the heat sink surface and in the computational domain where the time cost and the result accuracy are acceptable.

5 Emissivity Results

Figure 5 shows the comparison of total hemispherical emissivity between die-cast A380 Al alloy and the machined Al alloy 6061. The surface of die-cast aluminum had an emissivity of 0.14 compared to the machined aluminum, which was 0.03. This is consistent with the typical range of emissivity for metals that are from 0.1 to 0.4 for unpolished and 0 to 0.2 for polished [29]. These values indirectly indicate the potential for improving radiation heat transfer for bare die-cast aluminum heat sinks. Given the fact that the die-cast procedures require molten metal been injected directly into a mold with high pressure, the oxidation process may have been expedited and intensified and resulted in a thicker oxide layer leading to the relative high emissivity. As for the machined Al alloy 6061 surface, the machining work certainly increases the overall surface roughness but not able to compensate for the thinner oxide layer as a result of machining. Overall, the measured emissivity of the machined aluminum surface would have less thermal radiation contribution to the overall heat transfer. The spectral distribution of surface emittance can be found in Ref. [30].

The total hemispherical emissivity values for a range of anodized die-cast aluminum are shown in Fig. 6. Type II-black treatment has the highest thermal emissivity of 0.92 while the type II-clear, type III-clear, and type III-clear unsealed increase the thermal emittance from bare die-cast aluminum surfaces to 0.86, 0.92, 0.91, respectively. Compared with the untreated surfaces, aluminum anodization could significantly improve the surface radiative emissive properties, up to seven times, regardless of treatment types. The comparison between the dyed and undyed samples, i.e., type II-black and type II-clear, shows a 5% enhancement in thermal emissivity. This is a combined effect from the use of pigments as well as the thickness of the AAO layer where both may contribute to the emissivity improvement. Despite the difference in the anodizing process, the anodized surfaces by type III-clear treatment have almost the same thermal emittance as type II-black. In addition, the results also show the influence of sealing on the thermal emissivity. The cold nickel fluoride sealing method used by the surface finishing vendor may help the thermal emissivity of the AAO layer resulted from type III treatment slightly increase from 0.91 to 0.92 but it falls into the range of measurement uncertainty. Previous studies on various sealing methods on the thermal emissivity [23] concluded that this may be attributed to the nature of the precipitated sealants.

The results for the anodized machined Al alloy 6061 sample surfaces are presented in Fig. 7. The same improvement of total hemispherical emissivity can be achieved but with slightly lower max value compared to the anodized die-cast samples. Type II-black

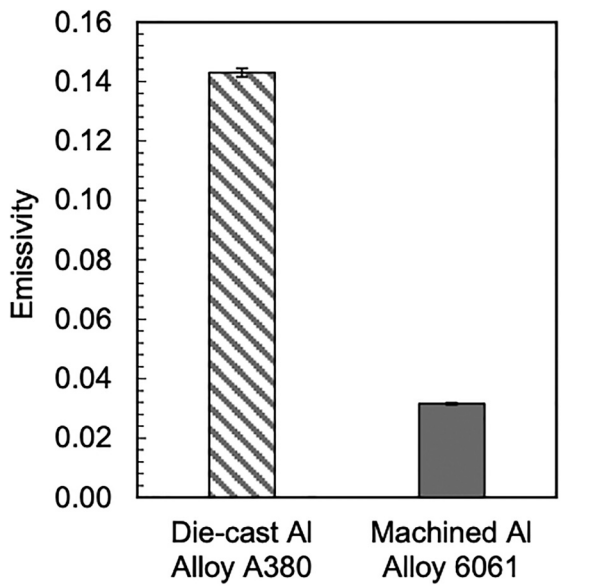

Fig. 5 Total hemispherical emissivity of the surface of die-cast, and machined aluminum

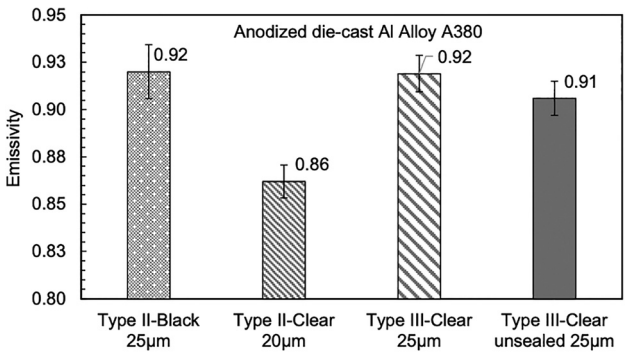

Fig. 6 Total hemispherical emissivity for various anodized die-cast Al alloy A380 sample surfaces

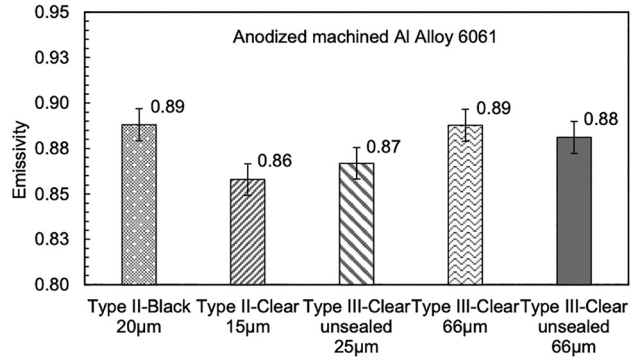

Fig. 7 Total hemispherical emissivity for various anodized machined Al alloy 6061 sample surfaces

and clear anodized surfaces have thermal emissivity of 0.89 and 0.86, respectively. It shows the same trend as anodized die-cast samples, where the dyed surfaces always yield better performance. As for type III anodization on machined Al alloy 6061 surfaces, various samples are prepared that have different thickness and sealing conditions. The results show that the thermal emissivity can be improved from 0.87 to 0.89 after the thickness of the AAO layer is increased from 25 μm (0.001 in.) to 66 μm (0.0026 in.). It also shows that the sealing method has a positive impact on the thermal emissivity to some extent, which has also been observed in the anodized die-cast samples.

6 Surface Morphology

On anodized die-cast sample surfaces (type III-clear unsealed 25 μm), two different surface structures are recorded as shown in Fig. 8, i.e., (a) the hexagonal textures and (b) porous layer-stacked structures. Figure 8(*a*) indicates that the anodic layer consists of individual areas in hexagonal shape where distinct boundaries separate each. The unevenly distributed pores are scattered around and hard to distinguish from the flakes stacked on top of each other within the area. On the other hand, Fig. 8(*b*) displays a rather different surface structure where the AAO films appear to pile layer-by-layer with miniature pores over the surface. We postulate that the formation of those two distinguishable yet different surface structures can be expressed as the surface imperfection in case of porosity. This commonly exists in the die-cast alloys that can be caused by several mechanisms to form voids and fine grain textures when gas is being trapped and molten metal solidify at a different rate between the near-wall and internal regions; also, the inclusion of impurities can create porosity in the die-cast parts. Additionally, the die-cast aluminum alloys have fairly amount of nonmetal elements and impurities where the aluminum usually takes up only 80–90% of the compositions. The added constituents should have the undesired and opposite impact on the formation of anodic oxide (AAO) layer and account for the exceptional surface structure.

In terms of sealed AAO layers, Fig. 9 presents a similar microstructure against the unsealed layer. Figure 9(*a*) shows the completed surfaces after type II-black anodizing and (b) refers to the surface resulted from the type III-clear process. The boundaries that shape the cells are still partially visible on both surfaces from which it may indicate the thickness of sealant film is comparably thin. The stains or shadows on the dyed surface may be the residues of insufficiently absorbed coloring pigments that are attached on the surface due to the pore-less and layer-stacked microstructure. As for surface uniformity, type III-clear treated surface has comparatively high surface irregularity in contrast to the type II-black. It may indicate a potentially higher resistance to wear and corrosion.

Even with the different surface morphology observed on the completed surface finishes on the die-cast A380 Al alloy, the emissivity measurement results from Sec. 5 reveal the same improvement. What we may conclude from this observation is that the formation of aluminum oxidation or anodic oxidation lays the foundation for thermal radiative properties enhancement regardless of the auxiliary treatments, i.e., coloring and sealing, that may help to a limited extent.

The surface structures of anodizing machined Al alloy 6061 (type III-clear unsealed 66 μm) are including in Fig. 10. The same hexagonal areas observed previously in the die-cast samples are also visible but in a smaller scale. With a higher magnification of 10,000×, the extreme miniature pores with an average diameter less than 10 nm can be seen over the entire sample. The efforts have been done to apply the same magnification to the die-cast samples but we failed to observe any resembled structure. This explains the fact that Al alloy 6061 yielded finer and much even surface appearance compared with die-cast samples where the composition of aluminum alloys matters.

7 Results and Discussion

7.1 Experimental Results. The thermal test results of bare and anodized heat sinks are provided in this section. The reported values are averaged to all recorded thermocouple readings within

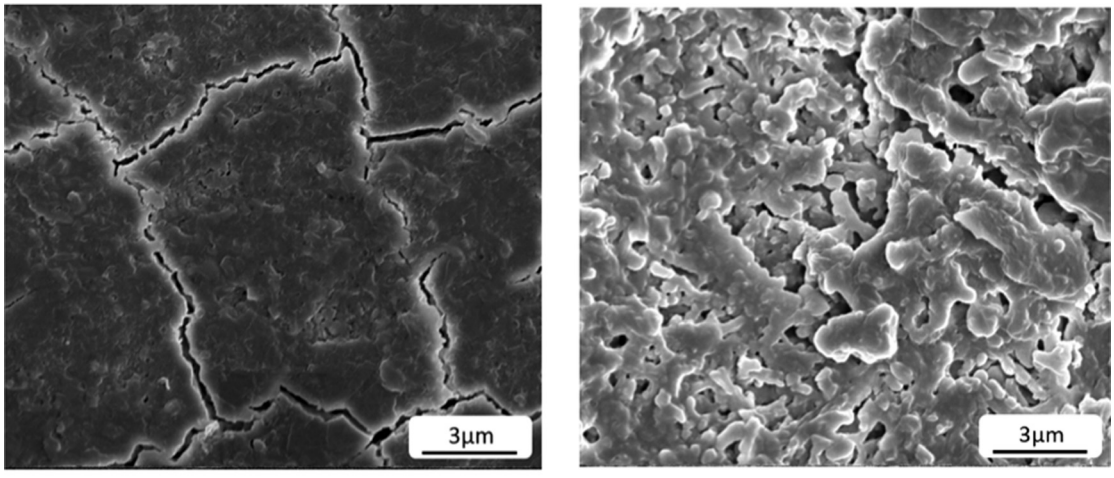

(*a*) (*b*)

Fig. 8 Two different surface morphology observed from unsealed anodic layer formed on die-cast Al alloy A380: (*a*) hexagonal textures; (*b*) porous and layer-stacked structures

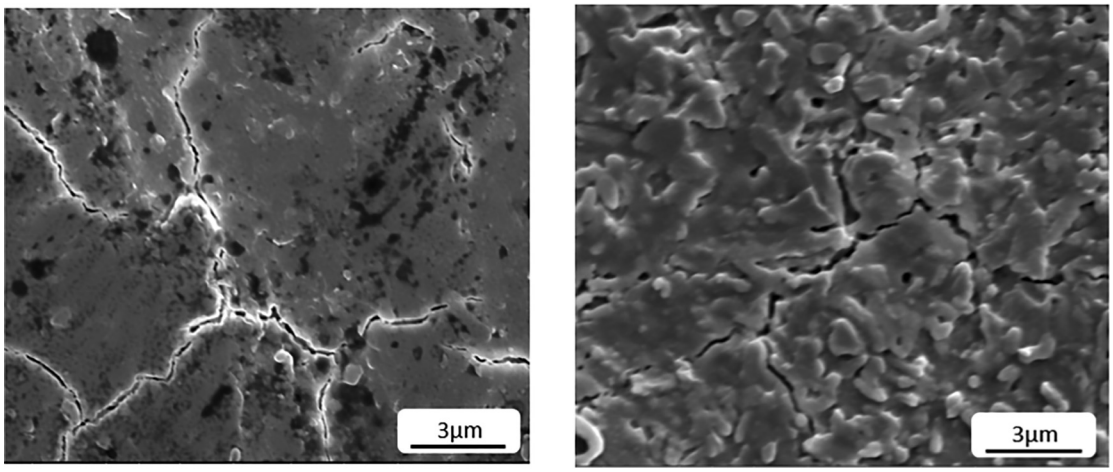

(*a*) (*b*)

Fig. 9 Surface morphology of sealed anodized surface formed on die-cast Al alloy A380: (*a*) type II-black and (*b*) type III-clear

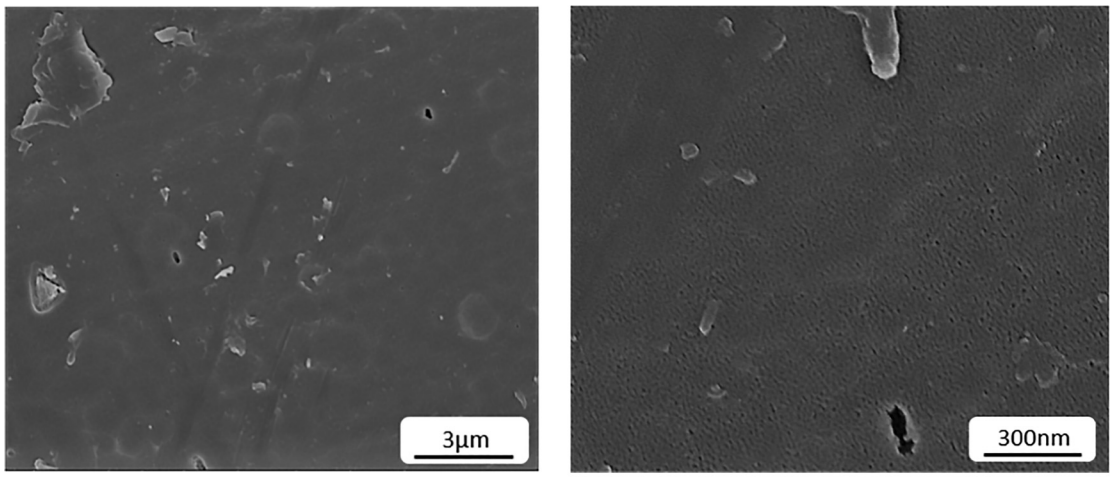

(*a*) (*b*)

Fig. 10 Surface morphology of unsealed anodized surface formed on machined Al alloy 6061

the last minute. The horizontal uncertainty bars represent the calculated error for input power measurements, which is ±1.7%. The vertical uncertainty bars are defined as the computed uncertainty for temperature measurement as well as thermal resistance. The uncertainty for temperature difference comprises of the accuracy of thermocouples, ±1.4 °C, and the standard deviations between tests. The maximum uncertainty for thermal resistance is calculated as ±6.4%.

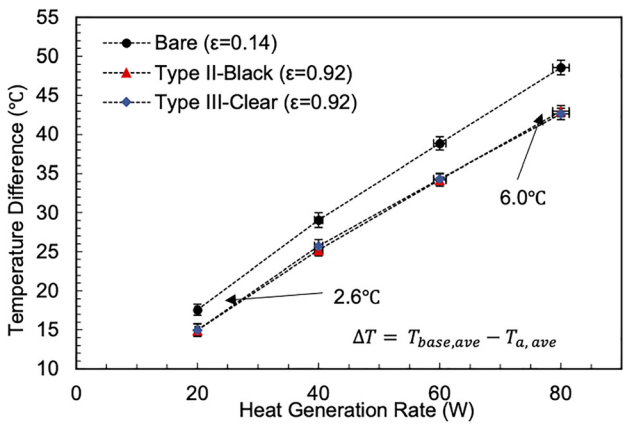

Fig. 11 Experimental data of average heat sink base temperature difference between the heat sink base and chamber ambient

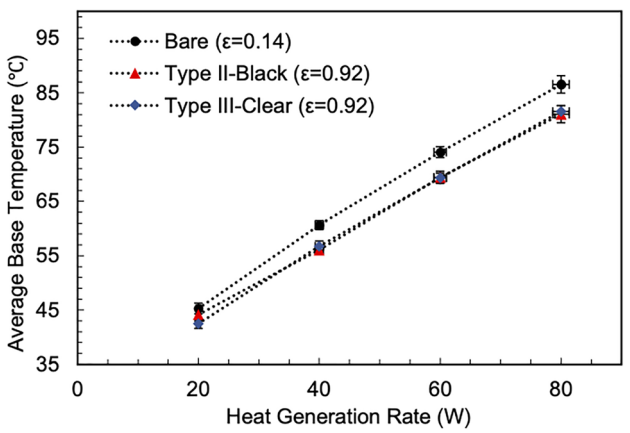

Fig. 12 Experimental data of average heat sink base temperature

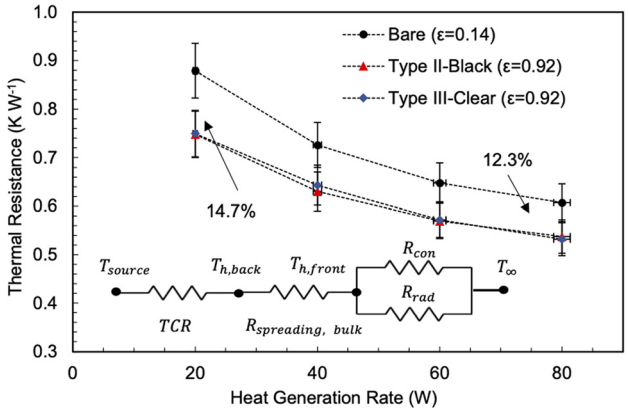

Fig. 13 Total thermal resistance in case of natural convection and thermal radiation from various tested heat sinks

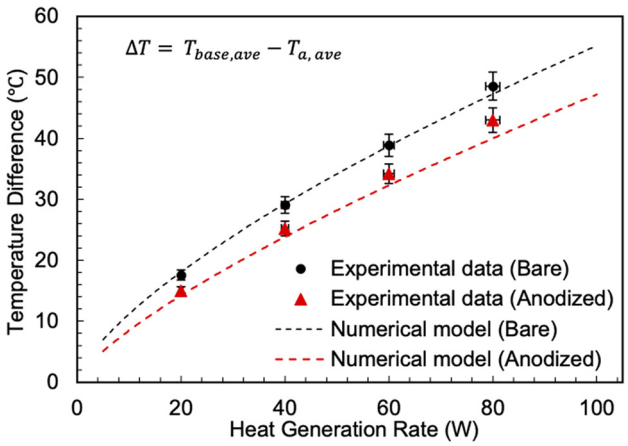

Fig. 14 Comparison of average heat sink base temperature with respect to ambient between the present numerical model (solid lines) and experimental data (solid symbols)

Figure 11 shows the average base temperature with reference to the average chamber ambient temperature and Fig. 12 represents the average heat sink base temperature. As shown, anodization significantly improves the overall thermal performance of treated heat sinks compared to the bare samples. The average base temperature difference drops approximately 6 °C, 12.3% in relative term, for the input of thermal power 80 W. Even for a thermal power of 20 W, a reduction of 14.7% in average base temperature can be seen where thermal radiation is expected to be minimized as the surface temperatures are lower.

Figure 13 shows the overall thermal resistance including both radiation and convection. It is defined between the average heat sink base temperature and the total heat generation rate as

$$R = \frac{T_{\text{base, ave}}}{Q} \tag{10}$$

The results indicate that a significant improvement of 14.7% is achievable after anodization. The overall thermal resistance is reduced from 0.61 $\text{K}\cdot\text{W}^{-1}$ to 0.53 $\text{K}\cdot\text{W}^{-1}$ when the heat input is maintained at 80 W. This further confirms the crucial impact of anodization on the thermal radiation and the overall thermal enhancement of die-cast heat sinks. It should also be noticed that the thermal resistance for natural convection and thermal radiation is decreased drastically when the power input into the system is increased from 20 W to 80 W since the heat sink temperature is increased notably. Indeed, higher temperature gradient provides more driving force for the heat transfer, which in turn leads to a reduction of the overall thermal resistance as shown in Fig. 13. Nevertheless, the impact of anodization on the overall thermal resistance stays unaffected where a considerable enhancement could be found.

7.2 Numerical Results. Figure 14 shows the comparison between the numerical results and the experimental data in the form of the temperature difference between the average heat sink base and average ambient. The solid symbols represent the

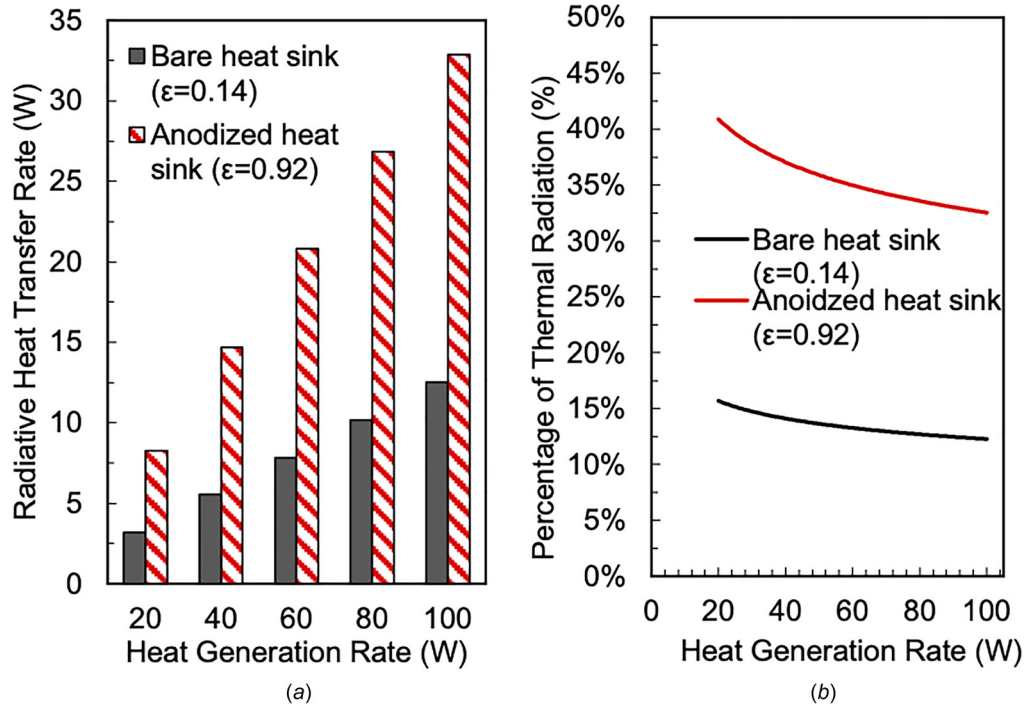

Fig. 15 Radiative heat transfer from the bare and the anodized heat sinks: (*a*) radiative heat transfer rate and (*b*) percentage of the thermal radiation in overall heat dissipation

measured values from various experiments and the solid lines denote the predictions from the numerical model. As shown, there is a good agreement between the numerical and experimental results with maximum relative differences of 2.1% and 7.0% in the case of surface emissivity of 0.14 and 0.92, respectively. After validation of the numerical model, it can be used to estimate the contribution of thermal radiative to the overall passive cooling capacity of such heat sinks.

The importance of thermal radiation in our naturally cooled heat sinks is shown in Fig. 15. The actual amount of the radiative heat transfer shows in Fig. 15(*a*) and the proportion of thermal radiation to the overall heat transfer is reported in Fig. 15(*b*). For bare heat sinks ($\varepsilon = 0.14$), the contribution of thermal radiation varies from 3.2 W (16%) to 12.5 W (12.5%) with increasing thermal power from 20 W to 100 W. As for anodized heat sinks ($\varepsilon = 0.92$), radiation plays a pivotal role as expected. For our heat sink, the amount of radiation increases from 8.3 W (41%) to 32.9 W (33%) for an input varying from 20 W to 100 W. This clearly indicates the potential for improving the radiation in naturally cooled heat sinks. The results also show that the radiation plays an even more important role when the temperature difference is smaller, i.e., where the driving force for natural convection is less substantial.

In addition, the experimental and numerical results show that the reduction in temperature difference has less impact on the combined thermal performance. The enhancement of surface emissivity not only can lead to a major improvement in thermal radiation but also is an effective means to expand the heat removal capacity of heat sinks, which is desirable and of numerous engineering applications.

8 Conclusions

A comprehensive study of surface radiative properties of anodized aluminum and their effects on thermal radiation from naturally cooled heat sinks is presented. The emissivity measurements suggest a great potential improvement can be achieved from all types of anodizing methods on either die-cast or machined aluminum alloys with a small variation of thermal emittance. A customized testbed was built and a series of anodized passively cooled heat sinks were tested. The experimental and numerical modeling results showed an increase of thermal emissivity on the heat sink surface can considerably reduce the surface average temperature, eliminate regions with relatively high temperature and increase the heat removal capacity. For this particular heat sink geometry, thermal ration can account for up to 41% of the overall heat dissipation.

Acknowledgment

The author would like to thank the kindly support from 4D LABs of SimonFraser University.

Funding Data

- Natural Sciences and Engineering Research Council of Canada (NSERC) Collaborative Research Development (Grant No. CRDPJ488777; Funder ID: 10.13039/501100000038).

Nomenclature

A = surface area (m^2)
c_p = specific heat ($J \cdot kg^{-1} \cdot K^{-1}$)
E = emissive power
F = view factor
H = heat sink height (m)
k = thermal conductivity ($W \cdot m^{-1} \cdot K^{-1}$)
L = heat sink length (m)
P = pressure (Pa)
q = heat flux ($W \cdot m^{-2}$)
Q = heat transfer rate (W)
r = surface distance (m)
R = thermal resistance ($K \cdot W^{-1}$)
t = time (s)
T = temperature (K)
TCR = thermal contact resistance ($K \cdot W^{-1}$)
u = velocity ($m \cdot s^{-1}$)
W = heat sink width (m)

Greek Symbols

α = thermal diffusivity ($m^2 \cdot s^{-1}$)
β = thermal expansion coefficient ($1 \cdot K^{-1}$)
γ = surface thermal reflectivity
Δ = difference
ε = surface thermal emissivity
θ = zenith angle (degree)
λ = wavelength (m)
ν = kinematic viscosity ($m^2 \cdot s^{-1}$)
ρ = density ($kg \cdot m^{-3}$)
σ = Stefan-Boltzmann constant (5.67×10^{-8} $W \cdot m^{-2} \cdot K^{-4}$)
φ = surface relative angles (degree)
ϕ = azimuthal angle (degree)

Subscripts

a, ∞ = ambient properties
ave = average properties
b = black body properties
back = heat sink back surface
base = heat sink base properties
bulk = bulk resistance
con = convective heat transfer
front = heat sink frontal surface
h = heat sink properties
measured = recorded spectrums for specimens
out = heat flux leaving the surfaces
r, rad = thermal radiative heat transfer
reference = recorded spectrums for polished gold
sample = sample properties
source = heat generation source
w = wall properties
zero = recorded spectrums for ambient
λ = spectral properties

Acronyms

AAO = anodic aluminum oxide layer
FTIR = Fourier transform infrared reflectometer
MTBF = mean time between failures
SAA = sulfuric acid anodized
URF = under relaxation factor

References

[1] Anandan, S. S., and Ramalingam, V., 2008, "Thermal Management of Electronics: A Review of Literature," Therm. Sci. **12**, pp. 5–26.
[2] Shabany, Y., 2010, *Heat Transfer: Thermal Management of Electronics*, CRC Press, Boca Raton, FL.
[3] Edwards, J., and Chaddock, J., 1963, "An Experimental Investigation of the Radiation and Free Convection Heat Transfer From a Cylindrical Disk Extended Surface," ASHRAE Trans., **69**(1), pp. 313–322.
[4] Rammohan Rao, V., and Venkateshan, S. P., 1996, "Experimental Study of Free Convection and Radiation in Horizontal Fin Arrays," Int. J. Heat Mass Transfer, **39**(4), pp. 779–789.
[5] Guglielmini, G., Nannei, E., and Tanda, G., 1987, "Natural Convection and Radiation Heat Transfer From Staggered Vertical Fins," Int. J. Heat Mass Transfer, **30**(9), pp. 1941–1948.
[6] Sparrow, E. M., and Vemuri, S. B., 1985, "Natural Convection/Radiation Heat Transfer From Highly Populated Pin Fin Arrays," ASME J. Heat Transfer, **107**(1), pp. 190–197.

[7] Rao, V. D., Naidu, S. V., Rao, B. G., and Sharma, K. V., 2006, "Heat Transfer From a Horizontal Fin Array by Natural Convection and Radiation-A Conjugate Analysis," Int. J. Heat Mass Transfer, **49**(19–20), pp. 3379–3391.
[8] Yu, S. H., Jang, D., and Lee, K. S., 2012, "Effect of Radiation in a Radial Heat Sink Under Natural Convection," Int. J. Heat Mass Transfer, **55**(1–3), pp. 505–509.
[9] Tamayol, A., McGregor, F., Demian, E., Trandafir, E., Bowler, P., Rada, P., and Bahrami, M., 2011, "Assessment of Thermal Performance of Electronic Enclosures With Rectangular Fins: A Passive Thermal Solution," ASME Paper No. IPACK2011-52174.
[10] Aihara, T., Maruyama, S., and Kobayakawa, S., 1990, "Free Convective/Radiative Heat Transfer From Pin-Fin Arrays With a Vertical Base Plate (General Representation of Heat Transfer Performance)," Int. J. Heat Mass Transfer, **33**(6), pp. 1223–1232.
[11] Lee, W., and Park, S., 2014, "Porous Anodic Aluminum Oxide: Anodization and Templated Synthesis of Functional Nanostructures," Chem. Rev., **114**(15), pp. 7487–7556.
[12] Sheasby, P. G., Pinner, R., and Wernick, S., 2001, *The Surface Treatment and Finishing of Aluminium and Its Alloys*, ASM International, Novelty, OH.
[13] Goeminne, G., Terryn, H., and Vereecken, J., 1995, "Characterisation of Conversion Layers on Aluminium by Means of Electrochemical Impedance Spectroscopy," Electrochim. Acta, **40**(4), pp. 479–486.
[14] Bouchama, L., Azzouz, N., Boukmouche, N., Chopart, J. P., Daltin, A. L., and Bouznit, Y., 2013, "Enhancing Aluminum Corrosion Resistance by Two-Step Anodizing Process," Surf. Coat. Technol., **235**, pp. 676–684.
[15] Harkness, A. C., and Young, L., 1966, "High Resistance Anodic Oxide Films on Aluminium," Can. J. Chem., **44**(20), pp. 2409–2413.
[16] Army Research Laboratory, 2003, "Anodic Coating for Aluminum and Aluminum Alloys (MIL-A-8625F)," accessed Feb. 18, 2020, https://quicksearch.dla.mil/qsDocDetails.aspx?ident_number=7074
[17] Bevans, J. T., Miller, W. D., Brown, G. L., Nelson, K. E., Luedke, E. E., and Russell, D. A., 1962, "An Investigation of the Thermal Radiation Properties of Certain Spacecraft Materials," National Aeronautics and Space Administration, Washington, DC, Report No. NASA-CR-74772, STL-8633-6014-SU-000.
[18] Lowery, J. R., and Marshall, G. C., 1977, "Solar Absorption Characteristics of Several Coatings and Surface Finishes," National Aeronautics and Space Administration, Washington, DC, Report No. NASA-TM-X-3509, M-218.
[19] Hemmer, J. H., 1984, "Solar Absorptance and Thermal Emittance of Some Common Spacecraft Thermal-Control Coatings," National Aeronautics and Space Administration, Washington, DC, Report No. NASA-RP-1121, REPT-84F0248, NAS 1.61:1121.
[20] Golden, J. L., 1993, "Anodized Aluminum on LDEF," LDEF Materials Results for Spacecraft Applications, National Aeronautics and Space Administration, Washington, DC, Report, pp. 61–71.
[21] Tribble, A. C., Lukins, R., Watts, E., Naumov, S. F., and Sergeev, V. K., 1995, "Low Earth Orbit Thermal Control Coatings Exposure Flight Tests: A Comparison of U.S. and Russian Results," National Aeronautics and Space Administration, Washington, DC, Report No. NASA-CR-4647, NAS 1.26:4647.
[22] Siva Kumar, C., Sharma, A. K., Mahendra, K. N., and Mayanna, S. M., 2000, "Studies on Anodic Oxide Coating With Low Absorptance and High Emittance on Aluminum Alloy 2024," Sol. Energy Mater. Sol. Cells, **60**(1), pp. 51–57.
[23] Lee, J., Kim, D., Choi, C., and Chung, W., 2017, "Nano Energy Nanoporous Anodic Alumina Oxide Layer and Its Sealing for the Enhancement of Radiative Heat Dissipation of Aluminum Alloy," Nano Energy, **31**, pp. 504–513.
[24] Klampfl, B. F., 1998, "A Parametric Study of Sulfuric Acid Anodized 5657 Aluminum Alloy Coatings for Thermal Control Applications," Master's thesis, Rice University, Houston, TX.
[25] SPECTRAL, 2019, "The Process of Anodizing, Spectral Finishing," Spectral Finishing Inc., Surrey, BC, accessed, Jun. 20, 2019, https://spectralfinishing.ca/home/the-process-of-anodizing/
[26] ASTM-408-71(1996)e1, 1971, "Standard Test Methods for Total Normal Emittance of Surfaces Using Inspection-Meter," Annu. B. ASTM Stand., **71**, pp. 2–4.
[27] Jaworske, D. A., 2003, "Portable Infrared Reflectometer for Evaluating Emittance," AIP Conf. Proc., **504**, pp. 791–796.
[28] ANSYS, 2016, "Ansys Fluent Help Version 17.2," ANSYS Corp., Canonsburg, PA.
[29] C¸engel, Y. A., 2008, *Introduction to Thermodynamics and Heat Transfer*, High Education, McGraw-Hill, New York.
[30] Zhang, Z., 2019, "Passive Cooling System: An Integrated Solution to the Applications in Power Electronics," Master's Thesis, Simon Fraser University, Surrey, BC, Canada.